Multi-Objective Optimization of a Hypersonic Inlet Using Generalized Outflow Boundary Conditions in the Continuous Adjoint Method

H. L. Kline*,
Thomas D. Economon†, and Juan J. Alonso‡
Stanford University, Stanford, CA, 94305, USA

Supersonic combustion ramjets, or scramjets have the potential to facilitate more efficient transatmospheric flight and airplane-like operations of launch vehicles. Although these airbreathing engines benefit from the mechanical simplicity of using flow deceleration only rather than mechanical compressors to achieve the conditions necessary for combustion, many challenges exist in their design. Robust and efficient design of these vehicles can benefit from the application of surface sensitivities calculated through the adjoint method. This work presents the derivation of a generalized boundary condition for the continuous adjoint which allows optimization for arbitrary outflow-based objectives, expanding the range of objectives that this method can address and facilitating multi-objective and multi-disciplinary optimization. The results of using this framework to optimize for a balance of thrust and nozzle exit area using low fidelity models of the combustion and expansion processes downstream of the inlet geometry are presented.

Nomenclature

Symbols

Γ_∞	Farfield boundary of the fluid domain
Γ_e	Outflow boundary of the fluid domain
Ω	Fluid volume domain
S	Solid wall boundary
$\dot{m}$	Mass flow rate $[kg\ m^{-2}\ s^{-1}]$
$\mathcal{A}$	Cross-sectional area $[m^2]$
$\mathcal{F}_{un}$	Uninstalled thrust $[N]$
$\vec{v}$	Velocity vector $[m\ s^{-1}]$
c	Speed of sound $[m\ s^{-1}]$
f	Fuel fraction
M	Mach Number
P	Pressure $[Pa]$
R	Specific Gas Constant $[JK^{-1}kg^{-1}]$
T	Temperature $[^\circ K]$
u, v, w	Cartesian components of velocity $[m\ s^{-1}]$
b	Burner
e	Outflow boundary
i	Inflow boundary
t	Stagnation value

*Ph.D. Candidate, Department of Aeronautics & Astronautics, hlkline@stanford.edu AIAA Student Member.
†Postdoctoral Scholar, Department of Aeronautics & Astronautics, AIAA Senior Member.
‡Professor, Department of Aeronautics & Astronautics, AIAA Associate Fellow.

0	Freestream
10	End of nozzle/ expansion ramp
2	Entrance to isolator, end of inlet
3	End of isolator, entrance to combustor
4	Exit of combustor
$\mathcal{J}$	Lagrangian
Ψ	Vector of Adjoint variables
$\vec{n}$	Unit normal vector
$\vec{t}$	Unit tangent vector
A	Jacobian Matrix
F	Convective Flux
J	Objective Function
U	Vector of conservative variables
V	Vector of primitive variables
x, y, z	Cartesian coordinates $[m]$

I. Introduction

Supersonic combustion ramjets, or scramjets, have the potential to facilitate more efficient transatmospheric flight and airplane-like operations of launch vehicles. A scramjet is an airbreathing engine that uses the compression of air over the forebody and inlet to achieve the conditions necessary for supersonic combustion, using no mechanical compressor. These engines operate in hypersonic conditions, ranging from Mach 5 to Mach 10 at current levels of technology. Ramjets have flown up through Mach 5.5, and at Mach numbers of around that magnitude it becomes more efficient to use supersonic combustion.[1] Flight tests of the HIFiRE, X-51 and X-43A have had success in achieving positive thrust, while also highlighting the difficulties of designing hypersonic airbreathing engines[1–4]. Under the extreme pressure and heat experienced at these flight conditions, there is a high degree of shape uncertainty. Hypersonic vehicles for access to space are required to operate under a very large range of flight conditions, accelerating to an altitude where rocket propulsion takes over. In addition, the phenomenon of unstart which causes a sudden decrease in thrust is important to consider. Shape uncertainty, the risk of unstart, and the requirement to operate at a wide range of conditions provide additional motivation for efficient evaluation of sensitivities. Surface sensitivities as well as sensitivities to freestream conditions can be used for optimization, to provide gradient information to the construction of response surfaces or to probability distribution estimates, and to qualitatively view what areas of a geometry are more or less influential to the quantity of interest.

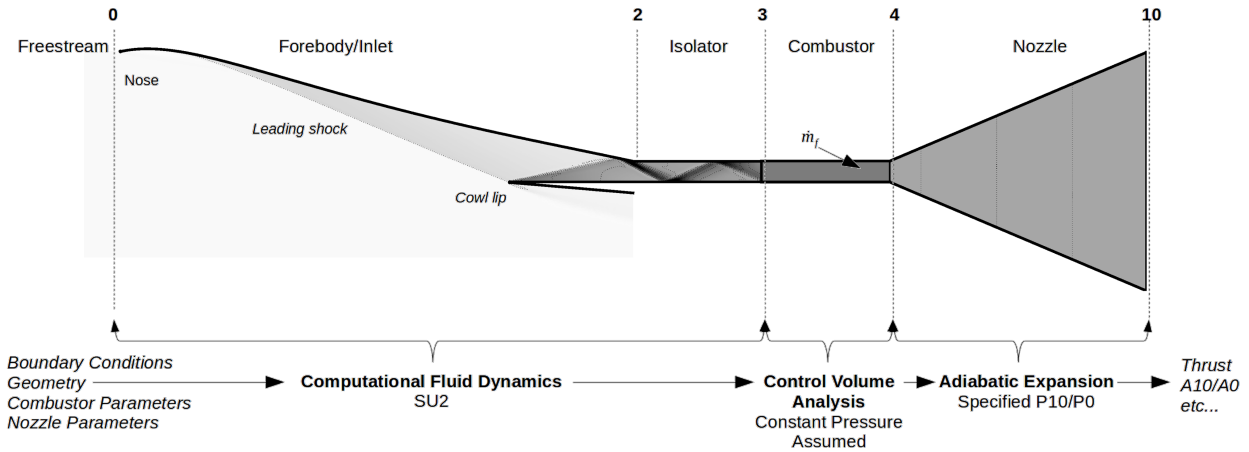

Figure 1: Scramjet flow path with station numbers indicated along top border of the image. Methods used to simulate each portion of the flow path are indicated along the bottom edge of the image. Contour levels are of pressure.

Modern simulation techniques allow for more efficient high fidelity optimization. Advances in computer speed and efficiency make it possible to complete more function evaluations than previously, however the cpu time required for high-fidelity optimization with large number of design variables is still significant. More efficient calculation of the gradient of the objective function(s) can significantly reduce the time required for optimization. The adjoint method introduced by Jameson[5] provides a more efficient method of calculating gradients, which is independent of the step size and of the number of design variables. The adjoint method is described further in Section II.B, and allows for the evaluation of gradients with respect to surface deformations without the need for mesh deformation and repeated CFD simulations for each design variable. An adjoint solution uses information from the direct, or flow solution, to solve a new partial differential equation system which produces analytical gradients to infinitesimal deformations of the surface. The gradients with respect to changes in freestream conditions can be found from the same adjoint solution. Adjoints have been applied to scramjet designs in the past, specifically Wang[6] et al. used a discrete adjoint for a pressure-based functional on the solid surface of a scramjet inlet to accelerate Monte-Carlo characterization of the probability of unstart.

The main contribution of this paper is the derivation and implementation of generalized continuous adjoint boundary conditions for outflow-based objectives. Commonly derivations of the continuous adjoint require a priori knowledge of the objective function desired. In this paper we show that the equations can be found for a generalized objective limited to functions of the density, velocity, static pressure, and problems where the outflow boundary remains undeformed. Implementing these boundary conditions for the case where area-averaged quantities are used, and implementing the tools necessary to communicate the required details of the externally defined objective function allows evaluating the surface sensitivity with respect to thrust without requiring CFD evaluation downstream of the inlet. For this work a mixture of methods will be used, summarized in Figure 1. These methods will be described further in Section II. This paper builds on previous work,[7] which used finite difference methods to evaluate the change in performance for a thermoelasticaly deformed inlet for an objective function of interest to a similar design problem. It is also based on work that derived the continuous adjoint boundary conditions for an objective of mass flow rate.[8] This work facilitates optimization of more complex objective functions, including objectives defined in an external script. This paper will begin with a description of the background, the design problem and geometry, followed by the methods used in this work including the derivation of the adjoint boundary conditions (Section II.B). Results of various optimization problems will be presented, along with conclusions related to their relevance for scramjet design.

I.A. Background

Hypersonic flow begins in the neighborhood of Mach 5, and is defined not with a specified Mach number but as the flight regime where a number of physical phenomena become more significant. These phenomena include thin shock layers where the shock lies very close to the surface of the vehicle, thick boundary layers which interact with the shocks and a large entropy gradient, and the possibility of chemically reacting flow and real gas effects.[9] Combustion at supersonic speeds is more difficult to achieve, and issues with residence time, sufficient mixing, and unstart become more significant. The inlets of scramjets need to compress the air sufficiently, while maintaining low drag and high efficiency. Figure 1 identifies the stations 0-10 which will be used as subscripts to describe the state of the flow at those locations. Several numbers are left out of this figure for consistency with other engine types which have more components. This figure shows the expansion component as a closed nozzle, however it should be noted that for many scramjet designs an expansion ramp is used. This does not effect the analysis used in this work, as only the area and pressure of the expanded flow is included.

There is ample existing work in the inverse design of inviscid inlets. A simple design is a two-dimensional single ramp which forms two shocks- the first extending from the nose of the vehicle and meeting the cowl, and the other returning the flow to the horizontal direction. A more efficient, but more difficult to implement alternative is the Busemann inlet,[10] which uses Mach waves to design a surface that isentropically compresses the flow up to a conical shock that returns the flow to horizontal. Stream tracing[11] techniques take advantage of the lower stagnation pressure losses of the Busemann inlet with an inlet geometry that can be more easily integrated. For example, a Rectangular to Elliptical Shape Transition[12] (REST) inlet transitions from a rectangular cross-section at the entrance to a circular cross-section at the combustor to gain benefits from simpler vehicle integration and lower weight combustors. However, even a REST inlet with boundary layer corrections may not achieve the designed performance[13] due to the complex interactions

of shocks and boundary layers in a complex internal hypersonic flow. This motivates the use of high fidelity optimization where those complex interactions can be taken into account in the design process.

For gradient-based optimization, there are multiple options available to provide the gradients. The finite difference method perturbs each design variable and re-evaluates the objective, while the continuous and discrete adjoint methods provide surface sensitivities which can be projected onto the individual design variables, requiring a single simulation in addition to the evaluation of the objective as opposed to requiring one evaluation per design variable. The discrete adjoint differs from the continuous adjoint in several ways. The discrete adjoint as implemented in the SU2 framework utilizes automatic differentiation of the initial CFD code to find an exact derivative of the inexact functional. This has some advantages in obtaining results that are generally much closer to finite difference results, however there are greater memory requirements required due to the larger amount of information needed during calculation. The continuous adjoint, by contrast, is sometimes more removed from finite difference and discrete adjoint result. The continuous adjoint solves the discretization of the linearized fluid problem, while the discrete adjoint solves the linearization of the discretized fluid problem. In other words, the continuous adjoint solves a problem defined by careful implementation of problem defined by taking the adjoint of the original un-discretized fluid problem. The discrete adjoint solves a problem defined by taking the adjoint of the already-discretized fluid problem. Theoretically, these methods should be equivalent if the discretization of both adjoint methods and the direct problem are perfect and if the numerical tricks such as limiters and other corrections were included in the continuous adjoint. Some work[14,15] has focused on making the discrete adjoint more efficient and expanding its capabilities. In this work, I am approaching the problem from the other direction - by making the boundary conditions of the continuous adjoint more general such that the numerical efficiency of the continuous adjoint can be utilized without as much of a limitation on the objective function. Arian & Salas[16] have also explored expanding the limits of what objectives can be addressed by the continuous adjoint, focusing on solid wall boundaries.

I.B. Design Problem

Several quantities of interest could be used for optimization. The choice of objective function will strongly determine the outcome. For inlet optimization, the stagnation pressure is often maximized, and there are several other options related to inlet performance such as the kinetic energy efficiency. Generally, the thrust is not directly used as an objective function due to the relative complexity of evaluating the function. In this work, we overcome that complexity through the generalized derivation of the adjoint boundary conditions and the use of low fidelity methods for the properties downstream of the isolator. The uninstalled thrust can be expressed as:

$$\mathcal{F}_{un} = \dot{m}_0 c_0 M_0 \left((1+f) \frac{M_{10}}{M_0} \sqrt{\frac{T_{10}}{T_0}} - 1 \right) + \frac{\mathcal{A}_{10}}{\mathcal{A}_0} \left(\frac{P_{10}}{P_0} - 1 \right) \tag{1}$$

In this equation M is the Mach number, P is the static pressure, T is the static temperature, f is the mass flow fraction of fuel:air, c indicates the speed of sound, $\mathcal{A}$ is the cross-sectional area, and $\dot{m}$ is the mass flow rate. The quantities with subscript 0 are the freestream values, and the quantities with subscript 10 are values at the exit of the nozzle or expansion ramp, as shown in Figure 1.

Flight conditions are Mach 7.0, dynamic pressure of approximately 85 kPa, and Reynolds number of approximately 5×10^6. These conditions correspond approximately to the HiFIRE flight 2 trajectory.[4] These conditions have been chosen to be reasonably representative of current scramjet technology.

II. Models

This section will describe the Computational Fluid Dynamics (CFD) tools used, the derivation of the adjoint equations and boundary conditions for the specific objective function used, the simulated geometry, and the one-dimensional evaluation of thrust.

II.A. Computational Fluid Dynamics

The open-source CFD suite SU2, developed in the Aerospace Design Lab at Stanford University,[17] was used to generate flow solutions and the adjoint solution. A new boundary condition and other modifications were

implemented in order to produce the continuous adjoint solution for generalized outflow-based objective functions. The Euler Equations were used in verification and in most optimization cases. The Reynolds-Averaged-Navier-Stokes (RANS) equations with the SA turbulence model was used for viscous simulations. The second order ROE scheme was used.

SU2 uses the Finite Volume Method (FVM) to solve partial differential equations on unstructured meshes. In the RANS equations, a turbulence model is used to account for the Reynolds stresses. The one-equation Spalart-Allmaras[18] and two-equation SST k-omega[19] turbulence models are available. The continuous adjoint equations are solved in a similar fashion, re-using methods implemented to solve partial differential equations and the information generated by the flow solver.

II.B. Adjoint Derivation With An Arbitrary Outflow-Based Objective Function

A continuous adjoint problem, using information from the direct, or flow solution, solves a new partial differential equation system which produces analytical gradients to infinitesimal deformations of the surface. The gradients with respect to changes in freestream conditions can be found from the same adjoint solution. The adjoint method requires a second PDE system and the derivation of boundary conditions that depend on the objective function of interest. While a new set of boundary conditions is required for every new objective function, this method provides gradients for an arbitrary number of design variables for approximately the same computational cost as a single additional direct solution. By comparison, the finite difference method of calculating gradients requires an additional direct solution for every additional design variable. A great deal of literature exists on adjoints and their derivation. The method was introduced by Jameson,[5] and further work by Giles & Pierce,[20] Castro[21] et al., Hayashi[22] et al., and Economon[23] provide additional details for the derivation and solution of adjoints. Papadimitriou & Giannakoglou[24] previously derived the adjoint for a total pressure objective function at an outlet. This work adds the derivation for a functional defined as an arbitrary function of the averaged flow properties at the exit.

When an adjoint is derived for an objective function J defined on some surface other than a solid body, it is called an off-body functional - for example, the mass flow rate $\dot{m}$ defined on the exit plane of an isolator. In these equations, U refers to the vector of conservative variables, $\vec{F}$ is the vector of convective fluxes, $\vec{A}$ is the convective jacobian, V is the vector of primitive variables, and M is the transformation matrix between the conservative and primitive variables. The jacobian and transfer matrices are expanded in the Appendix, Equations 32-35. W is the vector of characteristic variables, which are constant along characteristics of these equations. The transformation matrix L to characteristic variables is also shown in the Appendix. Ψ is the vector of adjoint variables. The adjoint variables, $\Psi = (\psi_\rho, \psi_{\vec{\rho v}}^T, \psi_{\rho E})^T$ are Lagrange multipliers for the direct system of equations, in this case the Euler Equations. Ω represents the volume.

Our objective function,

$$J = \int_{\Gamma_e} g ds, \tag{2}$$

is defined as an integral over an outlet surface Γ_e. The function g will be treated as a "black box". The conservative variables U and primitive variables V are defined as:

$$U = \left\{ \begin{array}{c} \rho \\ \rho\vec{v} \\ \rho E \end{array} \right\}, V = \left\{ \begin{array}{c} \rho \\ \vec{v} \\ P \end{array} \right\}. \tag{3}$$

Our goal is to find $\frac{\partial J}{\partial S}$, where S is the surface to be designed. In order to find this value, we set up a variational problem under the constraint that the variations of the flow variables must satisfy the direction problem. This constraint is satisfied by setting the variation of the residual $\mathcal{R}(U)$ to zero. Defining the Lagrangian for this problem and taking the first variation:

$$\begin{aligned} \mathcal{J} &= J - \int_\Omega \Psi^T \mathcal{R}(U) d\Omega \\ \delta\mathcal{J} &= \delta J - \int_\Omega \Psi^T \delta\mathcal{R}(U) d\Omega, \end{aligned} \tag{4}$$

where the adjoint variables Ψ are introduced as the Lagrange multipliers in the application of the constraint.

In order to solve this problem for the sensitivity $\frac{\partial \mathcal{J}}{\partial S}$, which will be equated to $\frac{\delta \mathcal{J}}{\delta S}$, we need to eliminate dependence on δU. This is accomplished first through linearizing the governing equations and applying known relationships between variables from the direct problem, and then through applying boundary conditions that eliminate the remaining undesired variational terms. Linearizing the direct problem and its boundary conditions and taking the first variation:

$$\begin{cases} \delta\mathcal{R} = \nabla \cdot \vec{A}\delta U & = 0 & \text{in } \Omega \\ \delta\vec{v} = -\partial_n(\vec{v})\ \delta S & & \text{on } S \\ (\delta W)_+ & = 0 & \text{on } \Gamma_\infty \\ \delta P & = 0 & \text{on } \Gamma_e \text{ where } M < 1 \end{cases} \tag{5}$$

In Equation 5, a constant pressure outlet is applied where the flow is subsonic, and the flow is tangent to solid walls. We now expand the variation of the objective J,

$$\delta J = \int_{\delta\Gamma_e} g(U)ds + \int_{\Gamma_e} \frac{\partial g}{\partial U}\delta U ds \tag{6}$$

Assuming that the outflow plane is undeformed such that the term $\delta\Gamma_e$ can be set to 0:

$$\int_{\delta\Gamma_e} g(U)ds = \int_{\Gamma_e} g(U)ds - \int_{\Gamma'_e} g(U)ds = 0 \tag{7}$$

This assumption simplifies the problem, and because the outflow boundary condition is defined in terms of pressure it is now convenient to restate the equation in terms of the primitive variables:

$$\delta J = \int_{\Gamma_e} \frac{\partial g}{\partial U}\delta U ds = \int_{\Gamma_e} \frac{\partial g}{\partial V}\delta V ds \tag{8}$$

Applying the Divergence Theorem to rewrite expression for $\delta\mathcal{J}$ from Equation 4,

$$\begin{aligned} \delta\mathcal{J} &= \delta J - \int_\Omega \Psi^T \delta\mathcal{R}(U)d\Omega \\ \int_\Omega \Psi^T \delta\mathcal{R}(U)d\Omega &= \int_\Gamma \Psi^T\vec{A}\cdot\vec{n}\delta U ds + \int_S \Psi^T\vec{A}\cdot\vec{n}\delta U ds + \int_S \Psi^T\vec{A}\cdot\vec{n}\delta S ds - \int_\Omega \nabla\Psi^T\vec{A}\delta U d\Omega \\ \delta\mathcal{J} &= \int_{\Gamma_e}\frac{\partial g}{\partial U}\delta U ds - \int_\Gamma \Psi^T\vec{A}\cdot\vec{n}\delta U ds - \int_S \Psi^T\vec{A}\cdot\vec{n}\delta U ds - \int_S \Psi^T\vec{A}\cdot\vec{n}U\delta S ds + \int_\Omega \nabla\Psi^T\cdot\vec{A}\delta U d\Omega, \end{aligned} \tag{9}$$

where Γ refers to the open boundary (farfield, inlet, and outflow boundaries), S refers to the solid surface, and Γ_e refers to the boundary over which J is calculated. Γ_e overlaps with Γ.

In order to find a solution for Ψ, we must make these equations independent of the variations δU. It is convenient at this point to use the primitive variables $\delta U = M\delta V$. On the boundaries, we use the boundary conditions from the direct problem to satisfy further conditions on δV - for example, at a subsonic outflow boundary with a fixed pressure, the variation in pressure is no longer arbitrary (and must be 0), resulting in a reduced number of equations that the adjoint variables must satisfy. The integral over the volume from Equation 9 defines the PDE to solve, and the integrals over the boundaries of the domain (Γ, S) provide the boundary conditions. A shorthand term will now be used for the momentum components of the adjoint variables, $\vec{\varphi} = \{\psi_{\rho u}, \psi_{\rho v}, \psi_{\rho w}\}^T$. The adjoint problem can now be summarized as:

$$\begin{cases} \nabla\Psi^T\cdot\vec{A} = 0 & \text{in } \Omega \\ \frac{\partial g}{\partial V}\delta V - \Psi^T\vec{A}\cdot\vec{n}M\delta V = 0 & \text{on } \Gamma_e \\ \Psi^T\vec{A}\cdot\vec{n}M\delta W = 0 & \text{on open boundaries } \Gamma \neq \Gamma_e \\ \vec{\varphi}\cdot\vec{n} = -\psi_{\rho E}\vec{v}\cdot\vec{n} & \text{on solid walls } S, \end{cases} \tag{10}$$

where the primitive variables have been used for convenience. These relations eliminate the dependence on δU from the final line of Equation 9. The remaining terms multiply δS and give the surface sensitivity.

Generalized Outflow Boundary Conditions with Fixed Back Pressure

The equations on the outflow boundary will now be used to find the boundary condition governing the adjoint variables for an arbitrary objective. Expanding the second line of Equation 10,

$$\left\{ \begin{array}{c} \frac{\partial g}{\partial \rho} \\ \frac{\partial g}{\partial \vec{v}} \\ \frac{\partial g}{\partial P} \end{array} \right\}^T \left\{ \begin{array}{c} \delta\rho \\ \delta\vec{v} \\ \delta P \end{array} \right\} - \left\{ \begin{array}{c} \psi_\rho v_n + \vec{v}\cdot\vec{\varphi}v_n + \psi_{\rho E} v_n \left(\frac{\vec{v}^2}{2}\right) \\ \rho(\vec{v}\cdot\vec{\varphi})\vec{n} + \rho v_n\vec{\varphi} + \rho\psi_\rho\vec{n} + \psi_{\rho E}\left(\rho v_n\vec{v} + \rho(\frac{c^2}{\gamma-1} + \gamma\frac{\vec{v}^2}{2})\vec{n}\right) \\ \vec{\varphi}\cdot\vec{n} + \psi_{\rho E}(v_n\frac{\gamma}{\gamma-1}) \end{array} \right\}^T \left\{ \begin{array}{c} \delta\rho \\ \delta\vec{v} \\ \delta P \end{array} \right\} \tag{11}$$

Under subsonic conditions the pressure at the outlet is specified, and therefore, $\delta P = 0$. Eliminating the dependence on the remaining, arbitrary, variations leads to:

$$\begin{aligned} \frac{\partial g}{\partial \rho} - \left(\psi_\rho v_n + \vec{v}\cdot\vec{\varphi}v_n + \psi_{\rho E} v_n\left(\frac{\vec{v}^2}{2}\right)\right) &= 0 \\ \frac{\partial g}{\partial \vec{v}} - \left(\vec{n}\left(\rho(\vec{v}\cdot\vec{\varphi}) + \rho\psi_\rho + \psi_{\rho E}\rho\left(\frac{c^2}{\gamma-1} + \gamma\frac{\vec{v}^2}{2}\right)\right) + \vec{\varphi}\left(\rho v_n\right) + \vec{v}\left(\psi_{\rho E}\rho v_n\right)\right) &= \vec{0} \end{aligned} \tag{12}$$

The boundary condition at the outlet in terms of the energy adjoint variable reduces to:

$$\left\{ \begin{array}{c} \psi_\rho \\ \vec{\varphi} \end{array} \right\} = \psi_{\rho E} \left\{ \begin{array}{c} \frac{2c^2+\vec{v}^2(\gamma-1)}{2(\gamma-1)} \\ -\vec{n}\frac{c^2}{v_n(\gamma-1)} - \vec{v} \end{array} \right\} + \left\{ \begin{array}{c} -\left(\frac{\partial g}{\partial \vec{v}}\cdot\vec{v}\frac{1}{\rho v_n}\right) + \left(\frac{\partial g}{\partial \rho}\frac{2}{v_n}\right) \\ \left(\frac{\partial g}{\partial \vec{v}}\frac{1}{\rho v_n} - \vec{n}\frac{\partial g}{\partial \rho}\frac{1}{v_n^2}\right) \end{array} \right\} \tag{13}$$

The remaining adjoint variable $\psi_{\rho E}$ is interpolated from the volume solution, often by taking the value at the nearest node in the volume (0^{th} order interpolation). When the exit experiences supersonic flow, δP becomes arbitrary, introducing an additional equation which can be solved to find the value of $\psi_{\rho E}$:

$$\psi_{\rho e, M>1} = \frac{\gamma-1}{v_n^2 - c^2}\left(\frac{\partial g}{\partial \rho}\frac{1}{v_n} + \frac{\partial g}{\partial P}v_n - \frac{\partial g}{\partial \vec{v}}\cdot\vec{n}\frac{1}{\rho}\right) \tag{14}$$

For the viscous case,

$$\psi^T\vec{A}\cdot\vec{n}\delta V + \psi^T\delta\left\{ \begin{array}{c} \cdot \\ \bar{\bar{\sigma}} \\ \bar{\bar{\sigma}}\cdot\vec{v} \end{array} \right\}\cdot\vec{n} + \psi^T\delta\left\{ \begin{array}{c} \cdot \\ \cdot \\ \mu_{tot}^2 c_p\nabla T \end{array} \right\}\cdot\vec{n} + \vec{n}\cdot\left(\Sigma^\varphi + \Sigma^{\psi_{\rho E}\vec{v}}\right) - \frac{\partial g}{\partial V}\delta V = 0, \tag{15}$$

could be applied, however for this work the perturbations of the viscous terms will be assumed negligible. This simplification is also assumed at farfield boundaries. This is a reasonable assumption because the gradients in the direction of the normal vector are expected to be small relative to other terms.

Generalized Characteristic-Based Outflow Boundary Conditions

Although the fixed pressure outflow boundary is used in this work, and is the boundary condition currently available in SU2, the alternative characteristic-based condition can be derived in the same way and will be presented here. The significance of the characteristic variables is that they result from the diagonalization of the Jacobians as shown in the Appendix. This allows us to derive the adjoint boundary conditions consistent with characteristic-based (Reimann) conditions in the direct flow problem. Because the supersonic case results in all characteristics exiting in the direct problem, and all entering in the adjoint problem, the resulting values of the adjoint variables will be the same. The difference is only relevant for the subsonic case and inside the boundary layer of viscous problems. Transforming the second equation of Equation Set 10 to

be in terms of characteristic variables W:

$$
\begin{aligned}
0 = \Psi^T \vec{A}\cdot\vec{n} M L \delta W - \frac{\partial g}{\partial U}^T M L \delta W = \Psi^T \vec{A}\cdot\vec{n} M L \delta W - \frac{\partial g}{\partial V}^T L \delta W \\
= \delta w_1 \left(-\frac{\partial g}{\partial \rho} + \frac{1}{2} v_n \left(2\psi_\rho + \vec{v}^2 \psi_{\rho e} + 2\vec{v}\cdot\vec{\varphi} \right) \right) \\
+\delta w_2 \left(\frac{\partial g}{\partial \vec{v}}\cdot\vec{n} + v_n \rho (\vec{\varphi}\times\vec{n} + \psi_{\rho e}\vec{v}\times\vec{n}) \right) \\
+\delta w_3 \left(\frac{-2}{4c} \left(c\frac{\partial g}{\partial \vec{v}}\cdot\vec{n} + c^2 \frac{\partial g}{\partial P}\rho + \frac{\partial g}{\partial \rho}\rho \right) \right. \\
\left. + \frac{\rho}{4c} \left(\psi_{\rho e} \left(\frac{2c^3\gamma}{\gamma-1} + 2c^2 (\frac{v_n \gamma}{\gamma-1}) + 2cv_n^2 \right) + (v_n + c) \left(2c(\varphi_n) + 2\psi_\rho + \vec{v}^2\psi_{\rho e} + 2\vec{v}\cdot\vec{\varphi} \right) \right) \right) \\
+\delta w_4 \left(\frac{-2}{4c} \left(-c(\frac{\partial g}{\partial \vec{v}}\cdot\vec{n}) + c^2 \frac{\partial g}{\partial P}\rho + \frac{\partial g}{\partial \rho}\rho \right) \right. \\
\left. + \frac{\rho}{4c} \left(\psi_{\rho e} \left(\frac{-2c^3\gamma}{\gamma-1} + \frac{2c^2 v_n \gamma}{\gamma-1} - 2cv_n^2 \right) + (v_n - c) \left(2\psi_\rho - 2c\varphi_n + \vec{v}^2\psi_{\rho e} + 2\vec{v}\cdot\vec{\varphi} \right) \right) \right)
\end{aligned}
\tag{16}
$$

For the subsonic case, $\delta w_4 = 0$ because that characteristic variable is associated with the negative characteristic speed $u - c$ from the direct problem, and so it is positive and exiting the volume in the adjoint problem. The remaining characteristics are entering the volume in the adjoint problem, and so their values are arbitrary. Setting the coefficients for the variation of the first three characteristics to 0 and solving for three of the adjoint variables:

$$
\begin{Bmatrix} \psi_\rho \\ \vec{\varphi} \end{Bmatrix} = \psi_{\rho e} \begin{Bmatrix} \frac{cv_n}{\gamma-1} + \frac{\vec{v}^2}{2} \\ -\vec{v} - \vec{n}\frac{c}{\gamma-1} \end{Bmatrix} + \begin{Bmatrix} \frac{1}{c+v_n} \left(\frac{\partial g}{\partial \rho}\frac{c+2v_n}{v_n} - cv_n \frac{\partial g}{\partial P} - \frac{\frac{\partial g}{\partial \vec{v}}\cdot\vec{v}}{\rho} - \frac{c(\vec{v}\times\vec{n})\cdot(\frac{\partial g}{\partial \vec{v}}\times\vec{n})}{\rho v_n} \right) \\ \frac{\vec{n}}{c+v_n} \left(\frac{\partial g}{\partial P}c - \frac{\partial g}{\partial \rho}\frac{1}{v_n} - \frac{\partial g}{\partial \vec{v}}\cdot\vec{n}\frac{c}{v_n \rho} \right) + \frac{\partial g}{\partial \vec{v}}\frac{1}{\rho v_n} \end{Bmatrix}
\tag{17}
$$

For the supersonic case, all of the characteristics of the adjoint problem are entering the volume, and so the value of its variation δw_4 is now arbitrary. This means that in order to solve for the adjoint variables the coefficient on this term must be set to zero, which provides an equation we can now solve for the remaining adjoint variable, $\psi_{\rho e}$:

$$
\psi_{\rho e, M_e > 1} = \frac{\gamma - 1}{v_n^2 - c^2} \left(\frac{\partial g}{\partial \rho}\frac{1}{v_n} + \frac{\partial g}{\partial P}v_n - \frac{\partial g}{\partial \vec{v}}\cdot\vec{n}\frac{1}{\rho} \right)
\tag{18}
$$

Note that the result for the supersonic case is identical. The supersonic solution for either boundary condition reduces to:

$$
\begin{Bmatrix} \psi_\rho \\ \vec{\varphi} \\ \psi_{\rho e} \end{Bmatrix} = \begin{Bmatrix}
\left(\frac{\partial g}{\partial \rho}\right)\frac{-2c^2+4v_n^2+\vec{v}^2(\gamma-1)}{2v_n(v_n^2-c^2)} & +\left(\frac{\partial g}{\partial \vec{v}}\cdot\vec{n}\right)\frac{2c^2+\vec{v}^2(\gamma-1)}{2(v_n^2-c^2)\rho} & +\left(\frac{\partial g}{\partial \vec{v}}\cdot\vec{v}\right)\frac{-c^2+v_n^2}{v_n(v_n^2-c^2)\rho} & +\left(\frac{\partial g}{\partial P}\right)\frac{-v_n(2c^2+\vec{v}^2(\gamma-1))}{2(c^2-v_n^2)} \\
\left(\frac{\partial g}{\partial \rho}\right)\frac{-\vec{n}-\vec{v}(\gamma-1)}{v_n^2-c^2} & +\left(\frac{\partial g}{\partial \vec{v}}\cdot\vec{n}\right)\frac{\vec{n}c^2+\vec{v}v_n(\gamma-1)}{v_n(v_n^2-c^2)\rho} & +\left(\frac{\partial g}{\partial \vec{v}}\right)\frac{v_n^2-c^2}{v_n(v_n^2-c^2)\rho} & +\left(\frac{\partial g}{\partial P}\right)\frac{\vec{n}c^2+\vec{v}v_n(\gamma-1)}{c^2-v_n^2} \\
\left(\frac{\partial g}{\partial \rho}\right)\frac{\gamma-1}{v_n(v_n^2-c^2)} & +\left(\frac{\partial g}{\partial \vec{v}}\cdot\vec{n}\right)\frac{1-\gamma}{\rho(v_n^2-c^2)} & & +\left(\frac{\partial g}{\partial P}\right)\frac{v_n(\gamma-1)}{v_n^2-c^2}
\end{Bmatrix}
\tag{19}
$$

Other Boundaries

At the inlet to the computational volume, boundary condition is defined by $\int_{\Gamma_i} (\Psi^T \vec{A}\cdot\vec{n}\delta U) ds = 0$ for the adjoint problem. In supersonic flow, all of the characteristics are exiting, leading to the condition that the adjoint variables are interpolated from the volume solution as the iterative solution progresses. At farfield boundaries, we assume that the variations of the conservative variables, δU are negligible, which is consistent with the boundary condition of the direct problem.

After application of the boundary conditions that eliminate the dependence on the variation in the conservative variables δU, and assuming only normal deformations, the remaining terms on the surface in

Equation 9 can be reduced to:

$$\begin{aligned}\delta\mathcal{J} &= \int_S \frac{\partial \mathcal{J}}{\partial S}\delta S ds \\ \frac{\partial \mathcal{J}}{\partial S} &= (\nabla\cdot\vec{v})(\rho\psi_\rho + \rho\vec{v}\cdot\psi_{\rho\vec{v}} + \rho H\psi_{\rho E}) + \vec{v}\cdot\nabla(\rho\psi_\rho + \rho\vec{v}\cdot\psi_{\rho\vec{v}} + \rho H\psi_{\rho E})\end{aligned} \tag{20}$$

This defines the surface sensitivity, $\frac{\partial \mathcal{J}}{\partial S}$, which is multiplied by the normal deformation δS. A full derivation of Equation 20 can be found in work by Castro.[21] The surface sensitivity is defined at every point on the surface assuming a continuous surface and continuous solution to the direct problem. In theory, the application of the divergence theorem during the derivation should require that discontinuities like shocks in the flow should be treated differently, e.g., by sensing the shock location and applying an additional boundary condition along that surface. In practice, as shocks are not true discontinuities within the numerical flow solution, this is not necessary, and gradients without a shock correction match well with finite difference results. It has also been assumed that viscous perturbations at the outlet, inlet, and farfield boundary conditions are negligible.

This derivation has focused on the inviscid problem. In the viscous problem, the boundary conditions on the surface and the equation for the surface sensitivity are modified. At inlet and outlet boundary conditions the viscous perturbations are assumed negligible, and these boundary conditions do not change. The equations defining these boundary conditions and the viscous surface sensitivity can be found in Reference [25]. Since the viscous perturbations at the outlet are neglected in this work, the boundary conditions developed here remain unchanged.

II.C. External Outflow-Based Objective Function

So far, the objective function has been treated entirely as a black box. This section will describe the low fidelity models used to model the flowpath downstream of the isolator. Area averages over the outflow of the isolator were used to link the CFD model to the one-dimensional or control volume models at Station 3 shown in Figure 1. Flux averaging,[26] which preserves the conservative variables, has been used in previous work.[8] However, area averaged values are more amenable to the derivation of the adjoint boundary conditions. The constant pressure combustion analysis was used for the results shown in this work because it produced conservative results relative to the constant area analysis for an initial design case, and its simplicity was more suited to testing the functionality of the generalized adjoint boundary conditions. The objective is expressed as a function of the averaged outflow values V,

$$\begin{aligned} J &= f(\bar{V}) \\ \bar{V} &= \frac{\int V ds}{\int ds}\end{aligned} \tag{21}$$

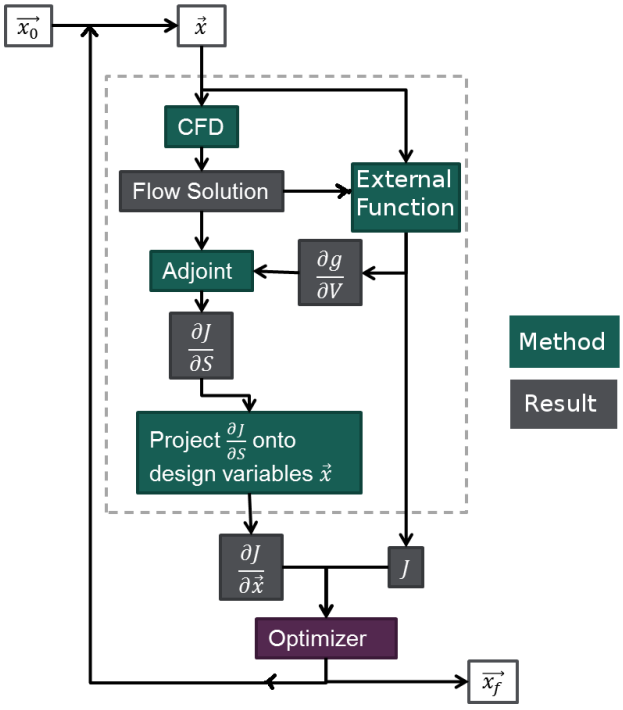

Figure 2: Flow chart showing relation of external script and CFD.

And so, the variation of the objective becomes:

$$\delta J = \int \delta V \frac{\partial f}{\partial \bar{V}}\frac{\partial \bar{V}}{\partial V} ds = \frac{\partial f}{\partial \bar{V}}\frac{1}{\int ds}\int \delta V ds, \tag{22}$$

where the term $\frac{\partial f}{\partial \bar{V}}$ is a constant, and the term δV is under the integral it can vary over the outflow boundary. We now need to relate this to the generalized outflow objective g as defined in Equation 2, which conveniently

results in constant values for the required gradients:

$$\frac{\partial g}{\partial V} = \frac{1}{\mathcal{A}_e}\frac{\partial f}{\partial \bar{V}} \tag{23}$$

Figure 2 illustrates the flow of information during the optimization loop. The design variables $\vec{x}$ are input into both the direct CFD solver and into the external/outside function, which also requires the flow solution to provide the gradients required for the adjoint solution and the evaluation of the objective function defined in the outside function. Because this "outside function" is implemented as a Python script, its details are very flexible, and new objective functions can be implemented without any need to recompile the SU2 C++ code. The gradients required for the boundary condition are found via finite difference within the python script, and passed into the configuration information for the adjoint simulation. The gradients can also be set manually within the configuration file.

Combustion Model

At station 4 of the flowpath through the engine, the air enters a combustion chamber. Conventionally, at this point fuel is mixed with the air, although in scramjet engines fuel may be added further upstream due to the greater difficulty of achieving complete mixing in the length of the combustor. Methods of mixing and adding fuel along the inlet surface have been studied by Turner[27] and found not to have a strong effect on the inlet performance, so for this work we will assume that the fuel and air are sufficiently mixed. High fidelity simulations exist for combustion processes,[28,29] as well as experimental results.[30] In this work, a 0^{th} order method will be used for the combustion and expansion processes. Since the adjoint boundary conditions have been derived such that the downstream model can be treated as a "black box," it would be theoretically possible, albeit more computationally expensive, to use higher fidelity methods to provide the values needed by the adjoint boundary conditions.

Constant pressure combustion assumes that the exit static pressure of the combustion chamber is equal to the entrance static pressure, $P_3 = P_4$. Using the conservation of, respectively, momentum, conservation of energy, and conservation of mass:

$$\begin{aligned}
u_4 &= u_3\left\{\frac{1+f\frac{u_{fx}}{u_3}}{1+f} - \frac{C_f\frac{\mathcal{A}_w}{\mathcal{A}_3}}{2(1+f)}\right\} \\
T_4 &= \frac{T_3}{1+f}\left\{1+\frac{1}{C_{pb}T_3}\left[\eta_b f h_{PR} + f h_f + f C_{pb}T^0 + \left(1+f\frac{u_f^2}{u_3^2}\right)\frac{u_3^2}{2}\right]\right\} - \frac{u_4^2}{2C_{pb}} \\
\frac{\mathcal{A}_4}{\mathcal{A}_3} &= (1+f)\frac{T_4}{T_3}\frac{u_3}{u_4}
\end{aligned} \tag{24}$$

Some values in these equations will have assumed values: the fuel injection axial velocity u_{fx} and the fuel injection total velocity u_f will be assumed negligible relative to u_3. The values of the remaining parameters can be found in the Appendix, Table 2.

Expansion Model

Adiabatic expansion to freestream pressure was assumed for the calculation of station 10 values based on the station 4 values computed from the combustion model. An expansion efficiency η_e and the pressure ratio $\frac{P_{10}}{P_0}$ are used in these equations. Ideal performance of the nozzle would occur with $\frac{P_{10}}{P_0} = 1.0$, and in fact this is assumed for optimization results where the parameters controlling the nozzle are not varied. However, for scramjets this would require an unfeasibly large nozzle, and so a ratio greater than 1.0 would be expected in realistic designs. The equations giving the properties at station 10 (the nozzle exit) as found in Heiser & Pratt[31] are:

$$\begin{aligned}
T_{10} &= T_4\left\{1-\eta_e\left[1-\left(\frac{P_{10}}{P_0}\frac{P_0}{P_4}\right)^{(R/C_{pe})}\right]\right\} \\
u_{10} &= \sqrt{u_4^2 + 2C_{pe}(T_4 - T_{10})} \\
\frac{\mathcal{A}_{10}}{\mathcal{A}_0} &= (1+f)\frac{P_0}{P_{10}}\frac{T_{10}}{T_0}\frac{u_0}{u_{10}}
\end{aligned} \tag{25}$$

II.D. Initial Design Geometry

A simple two-dimensional geometry used as an initial point for optimization. This geometry was designed using oblique shock equations[32] such that the shock resulting from the angle of the ramp meets the cowl lip. The height of the isolator and length of the cowl are designed such that the second shock impinges at the end of the ramp, leading to horizontal flow at the isolator. The parameters of this design are a desired static pressure ratio of 20.0, a design Mach number of 7.0, and an inlet length of 1.0 meters. The geometry is shown in Figure 3. The nose and cowl have been filleted to have a radius of 0.0005 meters in order to avoid sharp edges. Sharp edges, particularly when insufficiently resolved in the mesh, have been observed to result in poor quality results of the adjoint solution.

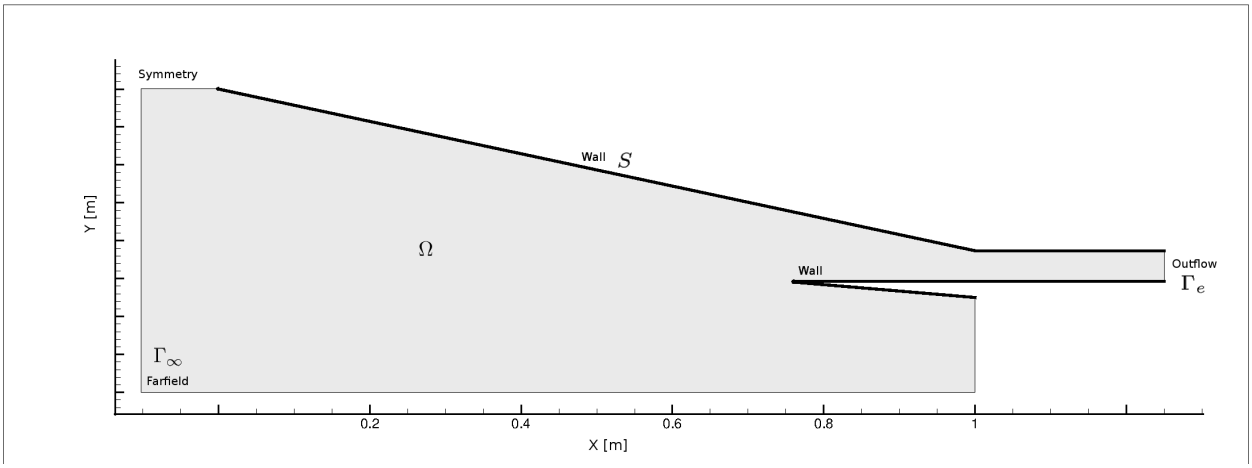

Figure 3: Baseline geometry used as initial point in optimization.

At Mach 7 in inviscid flow, the leading shock very nearly meets the cowl lip, and small amount of flow spillage occurs around the outer edge of the cowl due to the rounded edges of the geometry. As mass flow is a component of thrust, this is generally corrected by minor geometry modifications during optimization. The shock reflects off the cowl to meet the corner between the upper wall of the inlet and the isolator. A weak reflected shock can be observed within the isolator. Ideally, the flow would be turned exactly parallel to the isolator walls with no shocks within the isolator, and this weak shock train is due to the rounding of sharp edges of the geometry and numerical effects. In practice, a shock train would be expected in the isolator, as the idealized inviscid flow would not naturally occur. Optimization was also conducted on a three-dimensional geometry, shown in Figure 4. This geometry is an extrusion of the two-dimensional geometry shown in Figure 3. The total width is 0.1 m, with the simulated volume using a symmetry plane and 1/2 the total width.

Free-Form Deformation Variables

A Free-Form Deformation (FFD) strategy has also been adopted in both two and three dimensions, which has become a popular geometry parameterization technique for aerodynamic shape design.[33–35] In FFD, an initial box encapsulating the object (rotor blade, wing, fuselage, etc.) to be redesigned is parameterized as a Bézier solid. A set of control points are defined on the surface of the box, the number of which depends on the order of the chosen Bernstein polynomials. The solid box is parameterized by the following expression:

$$X(u,v,w) = \sum_{i,j,k=0}^{l,m,n} P_{i,j,k} B_j^l(u) B_j^m(v) B_k^n(w), \qquad (26)$$

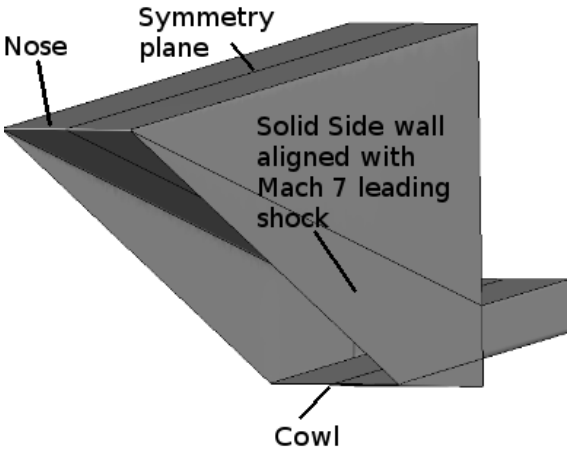

Figure 4: Three-dimensional initial geometry.

where u, v, $w \in [0, 1]$, and B^i is the Bernstein polynomial
of order i. The Cartesian coordinates of the points on the surface of the object are then transformed into parametric coordinates within the Bézier box.

The control points of the box become design variables, as they control the shape of the solid, and thus the shape of the surface grid inside. The box enclosing the geometry is then deformed by modifying its control points, with all the points inside the box inheriting a smooth deformation. Once the deformation has been applied, the new Cartesian coordinates of the object of interest can be recovered by simply evaluating the mapping inherent in Equation 26. An example of FFD control point deformation appears in Figure 5.

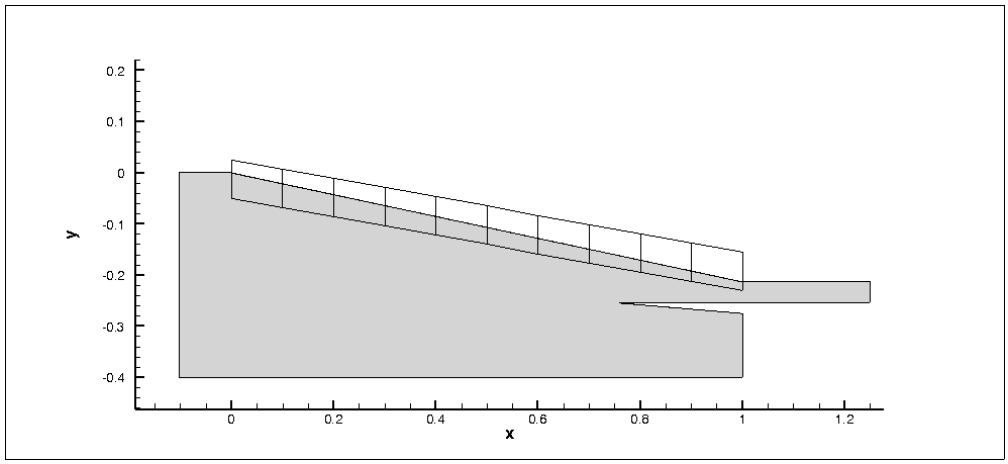

(a) Original inlet geometry and FFD bounding box with control points at the intersection of the black lines.

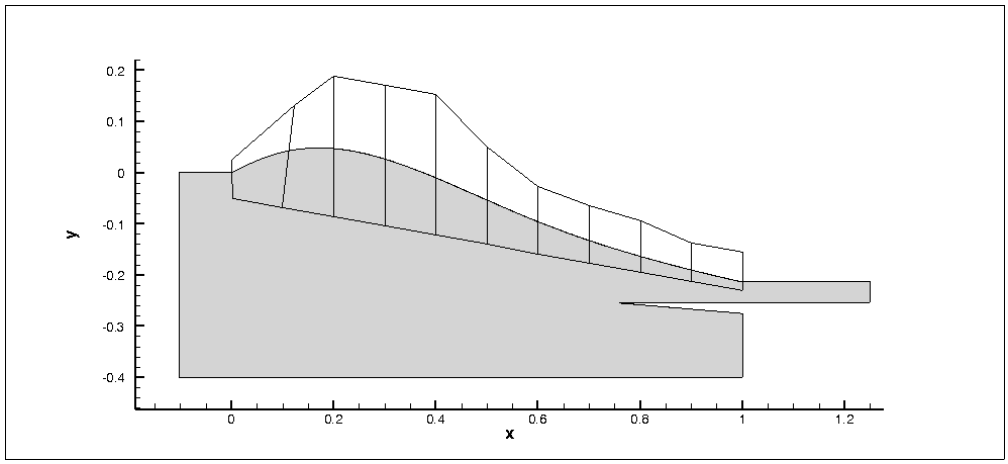

(b) Deformed inlet after displacement of the FFD control points near the compression ramp.

Figure 5: An example of the FFD technique applied to the two-dimensional inlet geometry.

II.E. Other Functionality Implemented in Support of This Work

Previously two-dimensional simulations experienced undesireable behavior during deformations near symmetry planes. In order to counteract this, code was implemented to constrain the symmetry boundary condition in two-dimensional simulations to deform only in the line of the boundary. Building on the work of Albring,[15] the necessary code modifications were implemented in this work to evaluate the discrete adjoint of outflow objectives of average total pressure, average static pressure, and mass flow rate. This allows comparison between the continuous and discrete adjoint computation of the pressure and mass flow rate objectives. Evaluating the discrete adjoint of the chain-rule based objective requires further work, specifically the modifications necessary to automatically differential the Python^{TM}-based model of the flowpath downstream of the inlet and isolator. A "Custom" design variable was also implemented to allow the use of additional design variables within the external script.

III. Results

In the preceding sections, the adjoint formulation for an arbitrary objective was derived, which facilitates the use a greater range of objective functions. The models used to estimate the thrust and other factors, for use as objective functions, were also presented. In this section, the gradients obtained using these equations will be checked against other methods: finite difference and discrete adjoint. The results of optimization studies will then be presented, including optimization results for simple objectives, a Pareto Front used to choose appropriate weighting for a two-objective problem, and results for a three-dimensional geometry optimized for a two-objective problem.

III.A. Verification of Outflow-Based Adjoint

For this work, boundary conditions for the continuous adjoint had been developed, and in this section the results of the continuous adjoint will be compared to results obtained using finite differences and/or the discrete adjoint. The discrete adjoint will only be included in comparisons where the objective is one of the area-averaged outputs from the CFD solution, since the capability to use external functions with the discrete adjoint is not implemented.

Verification Geometry

A simpler geometry was used to facilitate a grid refinement study, provide a smaller problem to facilitate running the larger number of CFD cases required for finite difference evaluations, and which matches geometry and flow conditions presented in literature.[36] The flow conditions are Mach 6.0, 470° K total temperature, and 10×10^6/m Reynolds number. The geometry is a 7.5° ramp 40 mm downstream of the leading edge. For this problem we assume a symmetry plan on the upper boundary, and the objectives will be defined on the right-hand plane of the volume shown in Figure 6. The FFD box used is also shown in Figure 6. The

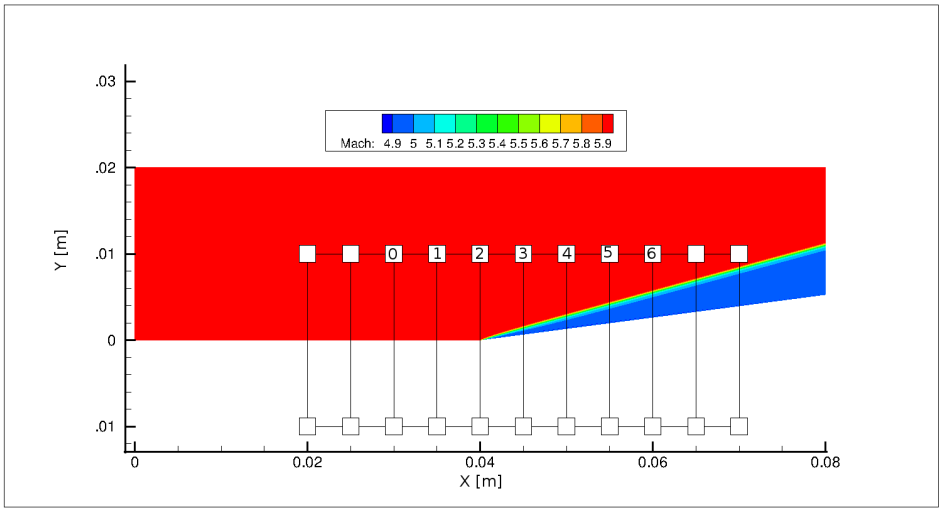

Figure 6: Geometry used for verification. Design variables are numbered at the associated FFD control point.

design variables are the 7 control points labelled 0 - 6.

Area-Averaged Static Pressure

Figure 7 compares the gradient calculated for area-averged static pressure using three different methods. The finite difference and discrete adjoint results are very close, as is expected. The continuous adjoint gradient is more removed from the finite difference and discrete adjoint results.

During the operation of the discrete and continuous adjoint for these cases, the memory usage of the computer cluster was observed. The average virtual memory per node was 3.6 times higher for the discrete adjoint problem on the same mesh and objective.

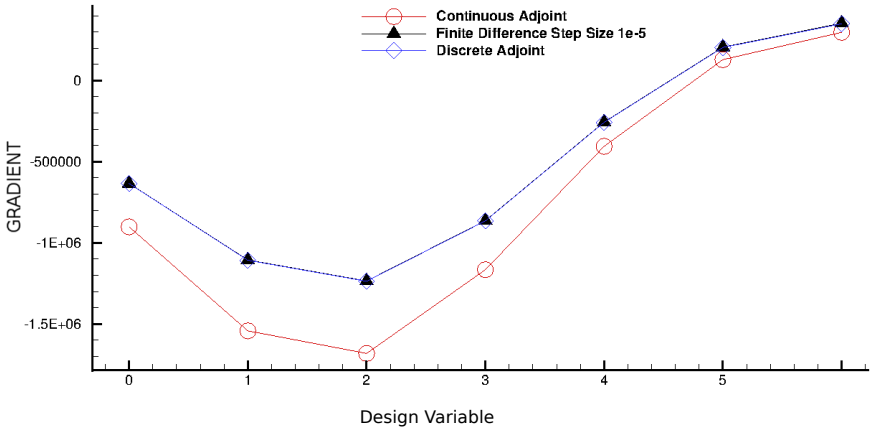

Figure 7: Gradient of area-averaged static pressure at the outflow of the isolator.

External Objective Function

Figure 8 compares the gradient of thrust defined in an external Python^{TM}script using the continuous adjoint and finite difference methods on the ramp case shown in Figure 6. These results show a match with the finite

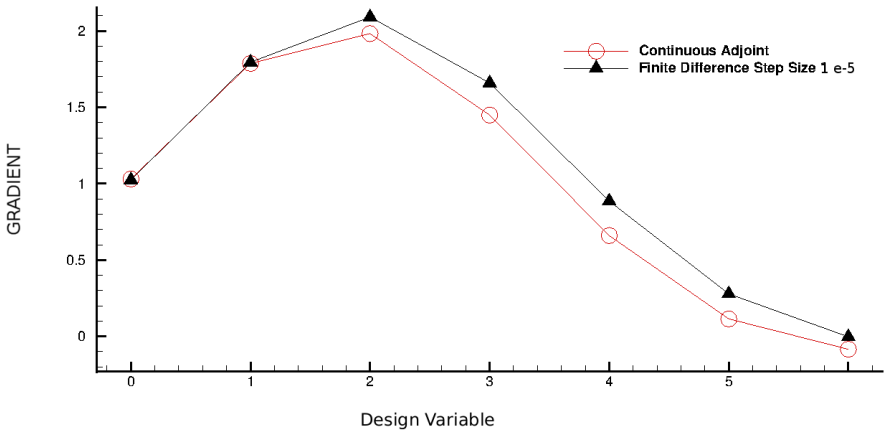

Figure 8: Gradient of function defined in an external script.

difference consistent with the match found for objectives defined within the $C++$ code, and so it appears that this method is appropriately finding the surface sensitivities for the external function.

III.B. Single-Objective Optimization: Thrust

To demonstrate the abilities of the generalized outflow-based adjoint for single-objective optimization, the thrust as defined in Equation 1 will be maximized;

$$\begin{aligned} &\min_{\vec{x}} J(\vec{x}) = -\mathcal{F}_{un} \\ &\text{subject to: } -0.2 \leq \vec{x} \leq 0.2 \end{aligned} \tag{27}$$

The design variables $\vec{x}$ are FFD control points, as illustrated in Figure 5.

The uninstalled thrust $\mathcal{F}_{un}$ is calculated by passing the area-averaged quantities into a Python^{TM}script which uses the models described in Section II.C to calculate the properties of the flow as it passes through

the combustion and expansion components. The resulting station 10 properties are used to find the thrust. The gradient of this value is then found by perturbing the station 3 quantities within the script to find the gradients of the function with respect to the primitive variables. These gradients are then passed into the continuous adjoint problem to find the surface sensitivities, which are projected onto the design variables $\vec{x}$. This would not be feasible without the generalized boundary conditions derived in this work.

2D Invsicid

The results in this section used thrust calculated using area-averaged outflow conditions as inputs into the control-volume analysis using constant pressure in the combustor and adiabatic expansion to freestream pressure. Figure 9 shows the flow at the initial point, and Figure 10 shows the flow after 6 major iterations and a 16% increase in thrust. Classically, we would expect designs to seek a weaker shock, making the initial

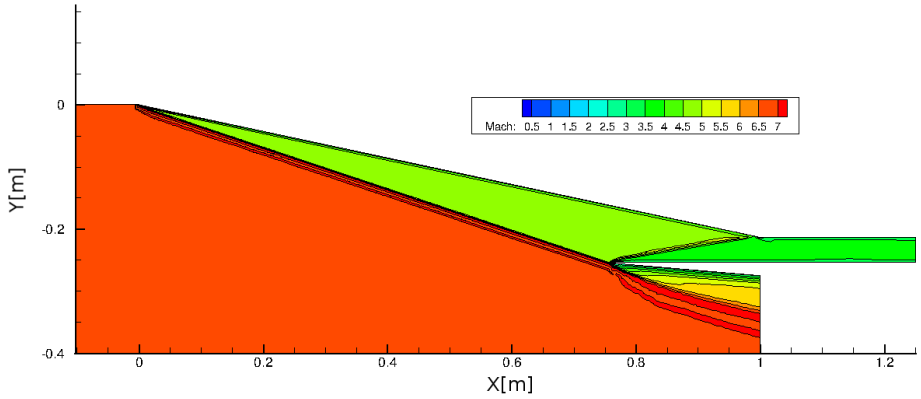

Figure 9: Initial design, inviscid flow at Mach 7.0

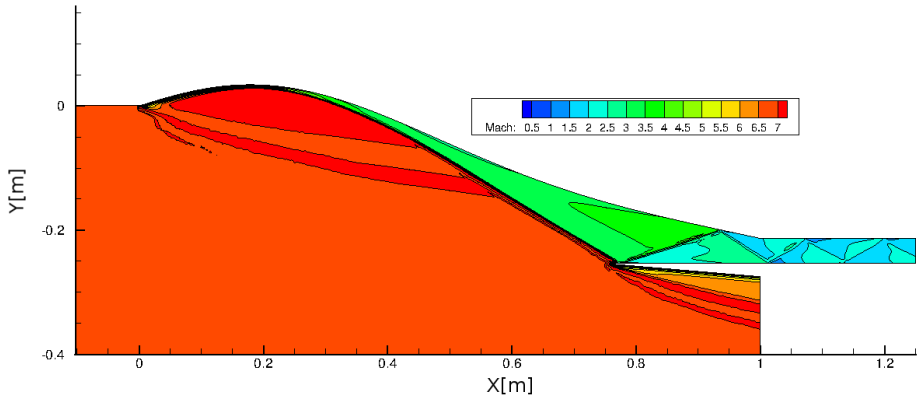

Figure 10: Geometry optimized for maximum thrust, inviscid flow at Mach 7.0

point in this optimization problem favorable. However, this solution has produced a stronger shock - and signficantly increased the thrust. While this particular geometry would cause some difficulty in integration into a larger vehicle and would likely suffer from separation at the nose in a viscous flow, the result of a stronger shock is still relevant. In order to prevent this extreme deformation it would be reasonable to use tighter bounds on the control points shown in Figure 5. This geometry has a lower compression efficiency, and yet a larger overall efficiency, as shown in Table 1. This is achieved due to the increase in static temperature and pressure at the entrance to the combustor, which increases the performance downstream of the inlet and outweighs the decreased inlet efficiency.

2D Viscous

The simulation of viscous flow is generally more computationally costly than inviscid flow. Due to the additional time required, it is beneficial to start from an initial point determined by the inviscid optimization rather than the initial straight ramp. Due to the large deformation applied during the inviscid optimization as shown in Figure 10, the viscous solution was not able to converge using the full deformation. Therefore, an initial point using 50% of the inviscid optimized geometry was used for optimization of thrust in viscous flow. Already, the thrust is improved by this deformed geometry relative to the original straight geometry. Relative to the viscous thrust on the straight geometry, the thrust has improved by 16.88%. The thrust

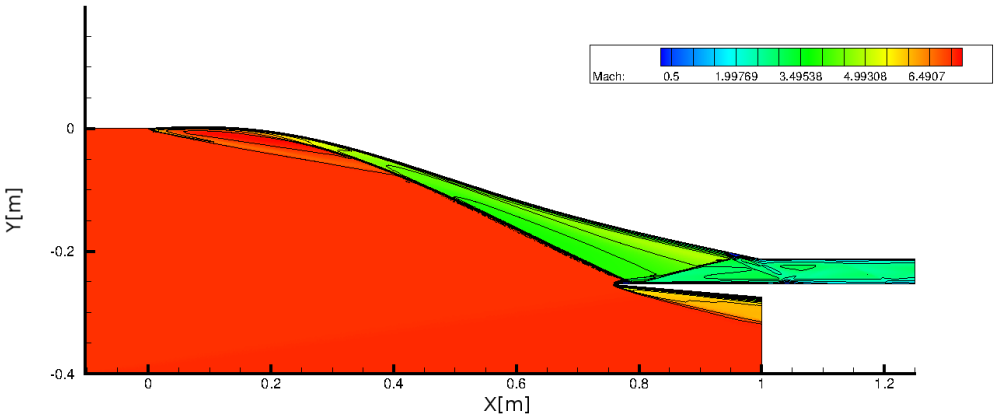

Figure 11: Initial design for viscous optimization of thrust, Mach 7.0

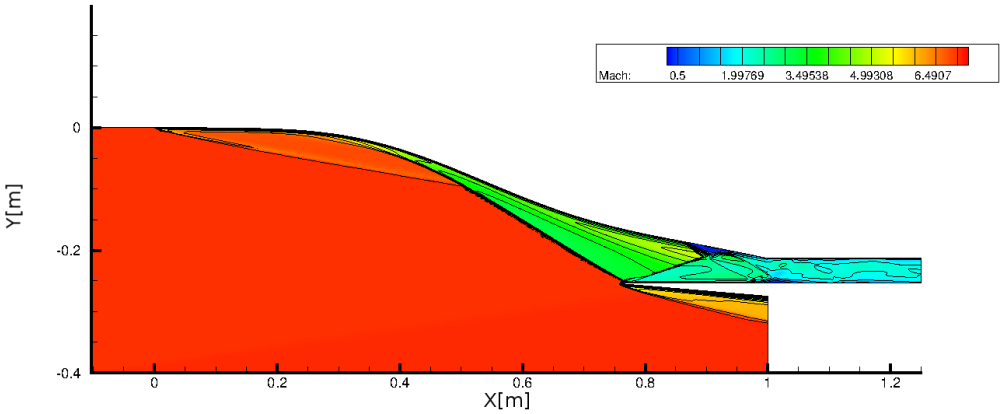

Figure 12: Geometry optimized for maximum thrust, viscous flow at Mach 7.0

is improved relative to the initial (predeformed) design shown in Figure 11 by 4.2 %, and relative to the straight initial geometry in viscous flow by 21 %. Qualitatively, the optimized geometry in Figure 12 has lengthened and straightened the front portion of the nose, effectively resulting in a sharper shock. It has also moved this shock such that it meets the cowl lip. As in the inviscid optimization problem, the optimizer has sacrificed compression efficiency in favor of higher thrust and therefore higher overall efficiency. It should also be noted that while dissociation effects were not included in this analysis, the temperature at the end of the inlet in the optimized case is $1333.5°K$, which is cause for some concern as air begins to dissociate around $2000°K$. Consideration of the dissociation of air within the combustor may be considered in future analyses. It is also interesting to note that a large separation region has been produces near the corner between the inlet and isolator where the reflected shock meets the wall. It would normally be assumed that such a separation region would detrimentally effect the inlet performance, but since in this case lower inlet efficiency is actually beneficial, to a certain extent, and assuming that the distortion of the flow is not

too extreme, this separation region may be acceptable. Considering that fuel mixing on the inlet has been considered for scramjets,[27] such a separation region may in fact be useful to the design.

III.C. Multi-Objective Optimization

The previous section showed the results of optimization with a single objective function. Although interesting, more complex optimization problems are now possible due to the implementation of generalized boundary conditions. The previous results assumed ideal expansion, which results in an infeasibly large nozzle area, on the order of 10× the capture area. In addition to hampering integration of the engine into the vehicle design, this large nozzle exit area also increases the structural weight. A reasonable multi-objective optimization will be comprised of both the thrust of the engine and the nozzle exit area. The nozzle exit area depends on the conditions at the end of the combustor, as well as on the extent to which the nozzle is under- or over-expanded. In order to add under-expansion as a design variable, additional changes were needed to the code to add the custom design variable of $\frac{P_{10}}{P_0}$ within the python script that calculates the thrust. All the results in this section are inviscid.

Overall Efficiency & Nozzle Area

The overall efficiency is defined as:

$$\eta_O = \frac{F_{un} V_0}{\dot{m} f h_{PR}} \tag{28}$$

The weighting function used for multi-objective optimization of a combination of the nozzle exit area and the overall efficiency is:

$$\begin{aligned} \min_{\vec{x},\, \frac{P_{10}}{P_0}} \; J_1(\vec{x}, \frac{P_{10}}{P_0}) =& - w_1 \eta_O + w_2 \frac{\mathcal{A}_{10} - 2.65}{2.65} \\ \text{subject to: } & w_1 + w_2 = 1 \\ & -0.2 \leq \vec{x} \leq 0.2 \\ & 1 \leq \frac{P_{10}}{P_0} \leq 5 \end{aligned} \tag{29}$$

The vector $\vec{x}$ is the set of FFD design variables. The area is normalized by its value at an initial point such that it will be on the order of 1.0. The initial point of the $\frac{P_{10}}{P_0}$ design variable was 3.0, and the initial deformations $\vec{x}$ were 0.

Figure 13 shows the resulting optimized geometries with a selection of values for w_1. The lengths of the combustor and nozzle are arbitrary - only the exit area is determined during this analysis. Very little change has occurred in the shape of the inlet, possibly due to there being no benefit to increasing $\dot{m}$ in this objective function. In terms of $\mathcal{A}_{10}$, as should be expected, a larger weight on η_O results in a large exit area and a larger weight on $\mathcal{A}_{10}$ results in a smaller area.

Thrust & Nozzle Area

The objective function used for a second multi-objective optimization is:

$$\begin{aligned} \min_{\vec{x},\, \frac{P_{10}}{P_0}} \; J_2(\vec{x}, \frac{P_{10}}{P_0}) =& - w_1 \frac{\mathcal{F}_{un}}{12000} + w_2 \frac{\mathcal{A}_{10} - 2.65}{2.65} \\ \text{subject to: } & w_1 + w_2 = 1 \\ & -0.2 \leq \vec{x} \leq 0.2 \\ & 1 \leq \frac{P_{10}}{P_0} \leq 5 \end{aligned} \tag{30}$$

This equation is a weighted sum of the thrust ($\mathcal{F}_{un}$) and the exit area, both normalized by their approximate value at the initial point such that the two objectives are both on the order of 1.0. A scaled thrust rather than overall efficiency is for comparison with the previous results. The initial point of the $\frac{P_{10}}{P_0}$ design variable was 3.0, and the initial deformations $\vec{x}$ were 0.

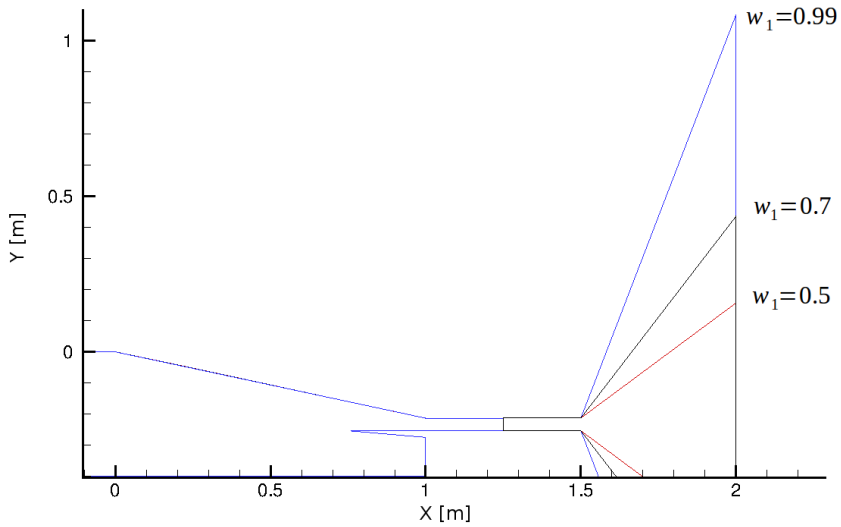

Figure 13: Multi-objective optimized geometries for η_o and $\mathcal{A}_{10}$ at a selection of weights. Nozzle area is symmetric about the centerline of the combustor. 1/2 area is shown for visualization.

Using the thrust rather than the overall efficiency resulted in a larger deformation applied to the inlet geometry, shown in Figure 14a. The different function has also changed the resulting nozzle areas. The lengths of the combustor and nozzle are arbitrary in these plots. Inspecting the geometry changes of the inlet in Figure 14b, although the nozzle area increases monotonically as the weight on the area portion of the objective decrease, the shape of the inlet varies with a similar general shape but without any easily recognized pattern as the weights on the objectives change. The individual optimization problems are generally converged, and the thrust increases monotonically, however the static pressure and temperature, as well as the stagnation pressure do not follow such a simple pattern, even between designs that have the same value of $\frac{P_{10}}{P_0}$. This highlights the nonlinearity of this problem. The exit area is effected both by the specified pressure ratio as well as by the outflow velocity and pressure at the end of the isolator.

A Pareto Front shown in Figure 15 was constructed using the two objective functions described, and shows the trade-off between overall efficiency η_O and the exit area A_{10}. The knee of this plot appears to be at approximately $\eta_O \approx 0.35$, $\mathcal{A}_{10} \approx 4 \times \mathcal{A}_0$, which is associated with a weight of $w_1 \approx 0.6$. More information such as the rate at which structural weight increases with respect to nozzle area would likely change this trade-off, particularly as the weight would affect the lift-induced drag. The overall efficiency at this choice of weights is reasonable as well. Higher efficiency for smaller areas may be possible with more design variables such as the inlet contraction ratio and/or three-dimensional effects, although these values are fairly consistent with literature.[37] As expected, although very high efficiencies may theoretically be possible, they come at the cost of unreasonably large nozzles. Practical designs generally include expansion ramps instead of enclosed nozzles to allow external expansion, however, the external expansion is then limited by the length of that ramp.

3D Inviscid

Based on the results of the two-dimensional multi-objective optimization, the three-dimensional geometry shown in Figure 4 was optimized for the objective shown in Equation 30, which is a balance of thrust $\mathcal{F}_{un}$ and exit area $\mathcal{A}_{10}$. A weighting of $w_1 = 0.5$ was used, and an initial pressure ratio of $\frac{P_{10}}{P_0} = 3$. This equation was adjusted to account for the span of 0.1 m by multiplying the constants by 0.1. This section will describe the results of this optimization. The design variables are illustrated in Figure 16. There are 25 FFD design variables, with axial deformations near the nose, vertical deformations along the ramp, and spanwise deformations near the outer edge of sidewall. The first step of the optimizer is shown in Figure 17. As with the two-dimensional case, the overall efficiency and thrust are increased. Due to the weighting chosen, the nozzle area has increased slightly. The overall efficiency and nozzle exit area are similar to the values produced with the same weights in the two-dimensional case. However, the compression efficiency

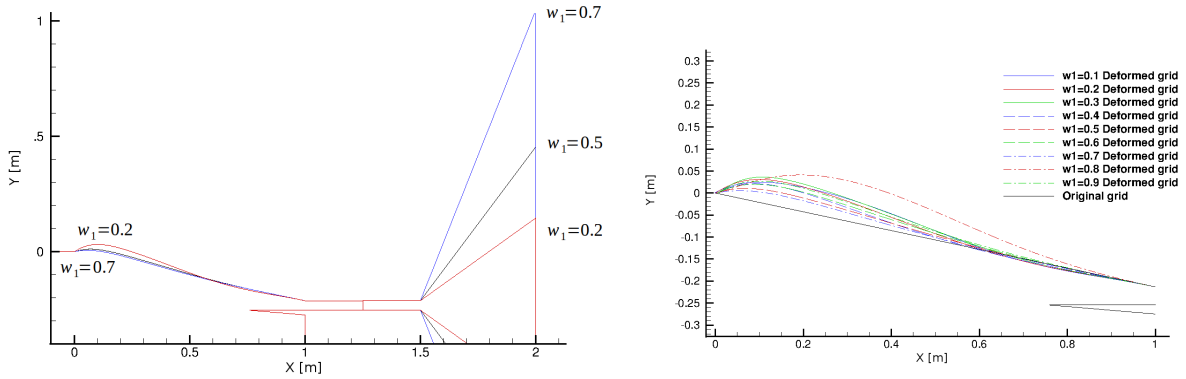

(a) Inlet and nozzle shapes. Nozzle area is symmetric (b) Inlet shapes detail comparing optimized geometries at about the centerline of the combustor. 1/2 area is shown various weights.
for visualization.

Figure 14: Multi-objective optimized geometries for $\mathcal{F}_{un}$ and $\mathcal{A}_{10}$ at a selection of weights.

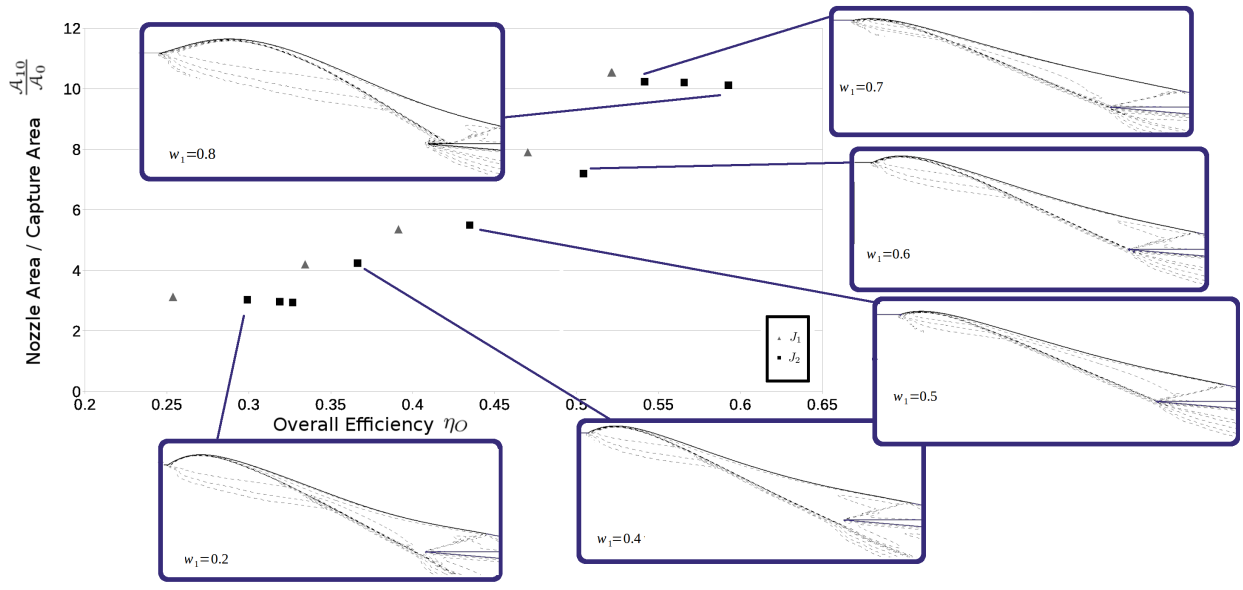

Figure 15: Pareto Front with results from two multi-objective optimizations.

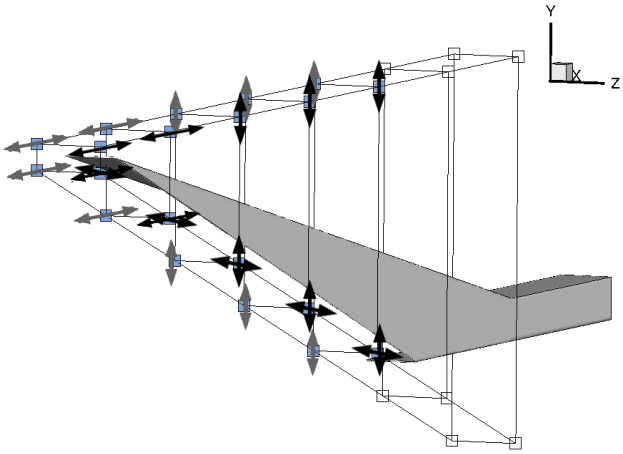

Figure 16: Three-dimensional optimization design variables. Arrows indicate the direction, with the variables on the symmetry plane shown in grey.

increases slightly, contrary to the two-dimensional results. This may be due to the larger number of design variables, to including the cowl in the available deformations, or due to three-dimensional effects. The static temperature and pressure at the end of the isolator are raised, which raises the efficiency of the combustor,[31] similar to the two-dimensional case. This also increases the pressure at the end of the nozzle, which has two competing effects: the thrust would increase if the nozzle area is kept constant, and a larger area ratio will result if the ratio $\frac{P_{10}}{P_0}$ is constant.

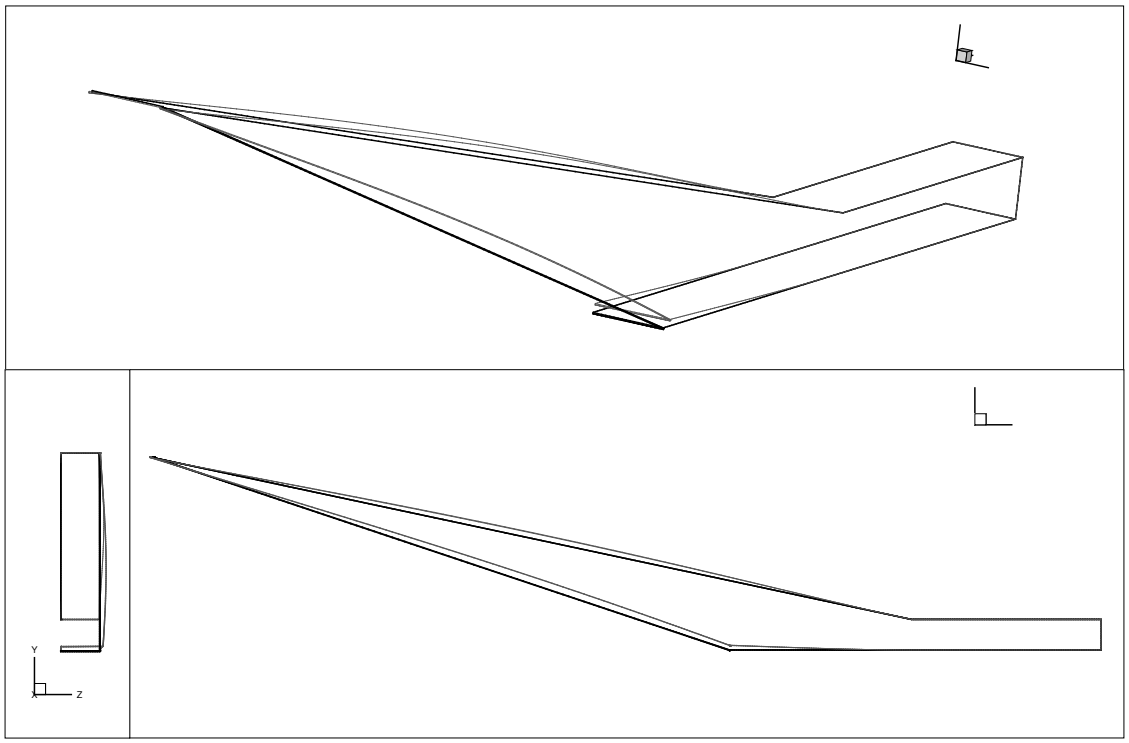

Figure 17: Three-dimensional optimization results, superimposing optimized geometry in grey on initial geometry.

III.D. Results Summary

Results of several of the cases discussed above are shown in Table 1. Some of the results to note are that the inviscid optimization achieves a significant improvement over the baseline, and that an improvement can be seen in the viscous case with 1/2 of the deformation from the inviscid optimization applied. In the multiobjective results, the exit area can be balanced against the uninstalled thrust. It should be noted that for scramjets an expansion ramp is often used, such that the exit area considered includes external expansion - this means that a larger exit area may still be feasible. The compression efficiency shown in Table 1 is defined as:

$$\eta_c = \frac{\frac{T_3}{T_0} - \left(\frac{P_{t0}}{P_{t3}}\right)^{(\gamma-1)/\gamma}}{\frac{T_3}{T_0} - 1}, \tag{31}$$

where P_t is the stagnation pressure. Usually this efficiency is defined over the inlet[31] (up to station 2 in Figure 1), however as the CFD in this work included an isolator portion this efficiency will be defined here using the station 3 values.

Case	Geometry	η_O	η_c	$\frac{\mathcal{A}_{10}}{\mathcal{A}_0}$	$\frac{P_3}{P_0}$	$\frac{P_{10}}{P_0}$	T_3 [° K]	Inlet Surface Drag [N]	$\mathcal{F}_{un}$ [N]
1. Inviscid Baseline	Figure 9	0.5886	0.8722	9.467	21.136	1	668.928	2.56E+003	1.77E+004
2. Inviscid Optimized for Thrust	Figure 10	0.6839	0.8147	8.73	58.147	1	1377.14	7.23E+003	2.06E+004
3. Viscous Baseline	N/A	0.597	0.8285	9.355	25.54	1	790.91	3.36E+003	1.79E+004
4. Viscous Flow, deformed by 50% of inviscidly optimized result	Figure 11	0.6309	0.82	8.969	39.795	1	1041.55	4.90E+003	2.10E+004
5. Viscous Optimized for Thrust	Figure 12	0.658	0.8108	8.774	58.079	1	1333.46	7.04E+003	2.19E+004
6. Inviscid Multi-Objective J_2, $w_1 = 0.1$	Figure 14a	0.3189	0.8086	2.962	42.853	5	1195.2	6.28E+003	9.60E+003
7. Inviscid Multi-Objective J_2, $w_1 = 0.5$	Figure 14a	0.4348	0.8346	5.4970	29.923	2.2274	869.4380	6.28E+003	1.31E+004
8. Inviscid 3D Baseline	Figure 17	0.3481	0.8800	4.5364	20.193	3.000	643.0190	1.27E+002	1.16E+003
9. Inviscid 3D Optimized for J_2	Figure 17	0.4244	0.8888	5.2229	22.715	2.404	708.4072	1.36E+002	1.41E+003

Table 1: Summary of Performance Results. Forces and areas for two-dimensional results are per-unit-span.

IV. Conclusion

A few conclusions can be found from Table 1. First of all, when optimizing for thrust, which includes the low-fidelity performance of combustion and expansion components, the efficiency of the compression component is actually decreased. In the first two rows of Table 1, we see that a decrease of 6% on the compression efficiency is correlated with an overall efficiency increase of 16% when optimizing the thrust. In Figure 10, we see that this is achieved by a dramatic, and potentially infeasible shape change. In fact, when simulating that geometry with viscous flow, the CFD solver was not able to converge, motivating the use of 50% of the deformation in Case 4 of Table 1. Optimization under viscous conditions shows similar results, an increase in overall efficiency and decrease in compression efficiency. The increase of the static pressure ratio when optimizing for thrust is consistent with work by Smart[37] which evaluated the level of compression

needed for increased performance using a lower fidelity model of the inlet and higher fidelity models of other components. Once multiple objectives are included, along with the addition of the design variable $\frac{P_{10}}{P_0}$, as seen cases 6 and 7 from Table 1, optimizing with a larger weighting on the nozzle area objective (case 6, $w_1 = 0.1$) results in a design that has lower overall efficiency as well as lower compression efficiency, but a more reasonable nozzle area. It should also be noted that as scramjets often use expansion ramps which allow external expansion, the area at station 10 would be the effective area of the expanding gas plume at the end of the expansion ramp rather than the enclosed area of a physical nozzle, making a larger area more feasible. Overall, these results show that the inclusion of the entire flowpath produces optimized solutions which are significantly different from optimizing for the compression component alone, and that the inclusion of multiple objectives further alters the design of the inlet. When the overall efficiency, which scales the thrust by mass flow rate and freestream values, was used in the objective function, very little change was seen in the inlet geometry. As it is know from the results of optimizing with thrust unscaled by mass flow rate that higher overall efficiency values are possible, the initial geometry may be a local minimum and/or the problem is sensitive to objective scaling and the chosen initial point.

A new generalized boundary condition for the continuous adjoint method has been presented, which facilitates more flexible outflow-based objectives. This formulation allows the continuous adjoint to be used for a much larger range of objectives than previous. Most often the continuous adjoint is used with a single surface-based objective, and sometimes a pressure-based outflow objective. While the continuous adjoint is still limited to objectives which allow the elimination of arbitrary variations during the derivation of the boundary conditions, the equations presented in this work greatly simplify the process of finding those boundary conditions for functions based on an integral over the outflow surface. Additionally, by treating this function as a "black box" in the implementation of the boundary condition, the adjoint problem can be used with a variety methods downstream of the outflow boundary. That is, while a simple model implemented in Python$^{\text{TM}}$has been used in this work, the same methods could also be used with higher fidelity models or with empirical models, as long as the required gradients are provided. Similar functionality may be possible with the discrete adjoint in SU2, but only with additional implementation and the potentially increased computational cost of that method.

This adjoint formulation was used to optimize a scramjet inlet geometry with respect to thrust and nozzle exit area objectives. Now that the ability to use a wider range of objective functions has been shown, more complex multiobjective problems can be addressed without changes to the compiled C++, as long as the problem is limited to outflow-based objectives. Future work will focus on expanding the capabilities of the adjoint method to be compatible with combinations of wall-based and outflow-based objectives, and to remove the limitation of functional dependence on only area-averaged quantities. In additional, consideration of unstart and gas dissociation may be included in the analysis of the flowpath downstream of the inlet.

V. Acknowledgements

This work was supported by a NASA Space Technology Research Fellowship. H. Kline would additionally like to acknowledge the support of the Hypersonic Airbreathing Propulsion Branch at NASA Langley in particular Shelly Ferlemann, the Aerospace Design Lab, and Stanford University.

References

[1]Hank, J. M., Murphy, J. S., and Mutzman, R. C., "The X-51A Scramjet Engine Flight Demonstration Program," *15th AIAA International Space Planes and Hypersonic Systems and Technologies Conference*, May 2008, pp. 1–13.

[2]Marshall, L., Bahm, C., Corpening, G., and Sherrill, R., "Overview With Results and Lessons Learned of the X-43A Mach 10 Flight," *AIAA/CIRA 13th International Space Planes and Hypersonics Systems and Technologies Conference*, May 2005, pp. 1–23.

[3]Jackson, K., Gruber, M., and Barhorst, T., "The HIFiRE flight 2 experiment: an overview and status update," *AIAA Paper*, Aug. 2009.

[4]Jackson, K. R., Gruber, M. R., and Buccellato, S., "HIFiRE flight 2 overview and status update 2011," *17th AIAA International Space Planes and Hypersonic Systems and Technologies Conference*, 2011, pp. 2011–2202.

[5]Jameson, A., "Aerodynamic Design via Control Theory," *Journal of Scientific Computing*, Vol. 3, No. 3, 1988, pp. 233–260.

[6]Wang, Q., Duraisamy, K., Alonso, J. J., and Iaccarino, G., "Risk assessment of scramjet unstart using adjoint-based sampling methods," *AIAA journal*, Vol. 50, No. 3, 2012, pp. 581–592.

[7]Kline, H., Palacios, F., and Alonso, J. J., "Sensitivity of the Performance of a 3-Dimensional Hypersonic Inlet to Shape

Deformations," *19th AIAA International Space Planes and Hypersonic Systems and Technologies Conference*, Atlanta, GA, June 2014.

[8]Kline, H., Palacios, F., Economon, T., and Alonso, J. J., "Adjoint-Based Optimization of a Hypersonic Inlet," *22nd AIAA Computational Fluid Dynamics Conference*, Dallas, TX, 2015.

[9]Anderson Jr., J. D., *Hypersonic and High-Temperature Gas Dynamics Second Edition*, AIAA Education Series, AIAA, Blacksburg, Virginia, 2nd ed., 2006.

[10]Busemann, A., "Die achsensymmetrische kegelige Überschallströmung," *Luftfahrtforschung*, Vol. 19, No. 4, 1942, pp. 137–144.

[11]Billig, F. S., Baurle, R. A., Tam, C.-J., and Wornom, S. F., "Design and analysis of streamline traced hypersonic inlets," *AIAA paper*, Vol. 4974, 1999, pp. 1999.

[12]Smart, M. K., "Design of Three-Dimensional Hypersonic Inlets with Rectangular-to-Elliptical Shape Transition," *Journal of Propulsion and Power*, Vol. 15, No. 3, May 1999, pp. 408–416.

[13]Gollan, R. and Ferlemann, P., "Investigation of REST-class Hypersonic Inlet Designs," *17th AIAA International Space Planes and Hypersonic Systems and Technologies Conference*, April 2011.

[14]Mader, C. A., Martins, J. R. R. A., Alonso, J. J., and van der Weide, E., "ADjoint: An Approach for the Rapid Development of Discrete Adjoint Solvers," *AIAA Journal*, Vol. 46, No. 4, April 2008, pp. 863–873.

[15]Albring, T., Sagebaum, M., and Gauger, N. R., "Development of a Consistent Discrete Adjoint Solver in an Evolving Aerodynamic Design Framework," *16th AIAA/ISSMO Multidisciplinary Analysis and Optimization Conference*, 2015, p. 3240.

[16]Arian, E. and Salas, M. D., "Admitting the Inadmissible: Adjoint Formulation for Incomplete Cost Functionals in Aerodynamic Optimization," *AIAA Journal*, Vol. 37, No. 1, 1999, pp. 37–44.

[17]Palacios, F., Colonno, M., Aranake, A., Campos, A., Copeland, S., Economon, T., Lonkar, A., Lukaczyk, T., Taylor, T., and Alonso, J., "Stanford University Unstructured (SU2): An open-source integrated computational environment for multi-physics simulation and design," *51st AIAA Aerospace Sciences Meeting and Exhibit.*, Grapevine, TX, Jan. 2013.

[18]Spalart, P. and Allmaras, S., "A one-equation turbulence model for aerodynamic flows," *AIAA Paper 1992-0439*, 1992.

[19]Menter, F., "Zonal Two Equation $k-\omega$, Turbulence Models for Aerodynamic Flows," *AIAA Paper*, Vol. 93-2906, 1993.

[20]Giles, M. B. and Pierce, N. A., "Adjoint equations in CFD : duality , boundary conditions and solution behaviour," *AIAA*, 1997.

[21]Castro, C., Lozano, C., Palacios, F., and Zuazua, E., "Systematic Continuous Adjoint Approach to Viscous Aerodynamic Design on Unstructured Grids," *AIAA Journal*, Vol. 45, No. 9, Sept. 2007, pp. 2125–2139.

[22]Hayashi, M., Ceze, M., and Volpe, E., "Characteristics-based boundary conditions for the Euler adjoint problem," *International Journal for Numerical Methods in Fluids*, Vol. 71, No. 10, 2012, pp. 1297–1321.

[23]Economon, T. D., *Optimal Shape Design Using an Unsteady Continuous Adjoint Approach*, Ph.D. thesis, Department of Aeronautics and Astronautics, Stanford University, 2014.

[24]Papadimitriou, D. and Giannakoglou, K., "Total pressure loss minimization in turbomachinery cascades using a new continuous adjoint formulation," *Proceedings of the Institution of Mechanical Engineers, Part A: Journal of Power and Energy*, Vol. 221, No. 6, 2007, pp. 865–872.

[25]Economon, T. D., Palacios, F., and Alonso, J. J., "An Unsteady Continuous Adjoint Approach for Aerodynamic Design on Dynamic Meshes," *AIAA Paper 2014-2300*, 2014.

[26]Baurle, R. and Gaffney, R., "The Art of Extracting One-Dimensional Flow Properties from Multi-Dimensional Data Sets," *AIAA*, Jan. 2007, pp. 1–19.

[27]Turner, J. C. and Smart, M. K., "Application of inlet injection to a three-dimensional scramjet at Mach 8," *AIAA journal*, Vol. 48, No. 4, 2010, pp. 829–838.

[28]Duraisamy, K. and Alonso, J., "Adjoint based techniques for uncertainty quantification in turbulent flows with combustion," *42nd AIAA Fluid Dynamics Conference and Exhibit*, 2012, p. 2711.

[29]Branch, H. A. P., "Numerical simulation of scramjet combustion in a shock tunnel," 2004.

[30]Rogers, R. C., Capriotti, D. P., and Guy, R. W., "Experimental supersonic combustion research at NASA Langley," *AIAA paper*, Vol. 98, 1998, pp. 2506.

[31]Heiser, W. H. and Pratt, D. T., *Hypersonic Airbreathing Propulsion*, AIAA Education Series, AIAA, Washington, D.C., 1994.

[32]Hirsch, C., *Numerical Computation of Internal and External Flows*, Vol. 2, John Wiley & Sons, 1990.

[33]Samareh, J. A., "Aerodynamic shape optimization based on Free-Form deformation," *AIAA Paper 2004-4630*, 2004.

[34]Kenway, G., Kennedy, G., and Martins, J. R. R. A., "A CAD-Free Approach to High-Fidelity Aerostructural Optimization," *AIAA Paper 2010-9231*, 2010.

[35]Anderson, G., Aftosmis, M., and Nemec, M., "Parametric Deformation of Discrete Geometry for Aerodynamic Shape Design," *AIAA Paper 2012-0965*, 2012.

[36]Simeonides, G., Haase, W., and Manna, M., "Experimental, analytical, and computational methods applied to hypersonic compression ramp flows," *AIAA journal*, Vol. 32, No. 2, 1994, pp. 301–310.

[37]Smart, M. K., "How Much Compression Should a Scramjet Inlet Do?" *AIAA Journal*, Vol. 50, No. 3, March 2012, pp. 610–619.

VI. Appendix

VI.A. Assumed Constants & Parameters

Table 2 summarizes the various parameter values assumed for the models used in this work. Many of the values are drawn from Heiser & Pratt.[31]

Parameter	Symbol	Value
Expansion Efficiency	η_e	0.9
Burner Efficiency	η_b	0.8
Constant pressure specific heat in burner and nozzle	$C_{pe} = C_{pb}$	1.51×10^3 J/kg K
Reference Temperature	T^0	222.0° K
Skin friction term	$\frac{C_f \mathcal{A}_w}{2\mathcal{A}_3}$	0.02
Enthalpy of Hydrogen Fuel	h_f	12.1×10^7 J/kg
Fuel mass fraction	f	0.0295
Product of mass fraction and combustion product enthalpy	$f \times h_{PR}$	3.510×10^6 J/kg

Table 2: Assumed Parameters

VI.B. Jacobians & Transfer Matrices

This section contains details of the Jacobian and other terms used in the derivation of the adjoint equations and boundary conditions. The Jacobians an transformation matrices are found in Hirsch[32] and are shown in the two dimensional form here.

Jacobian matrix for two dimensional Euler Equations:

$$A_x = \frac{\partial F_x}{\partial U} = \begin{bmatrix} 0 & 1 & 0 & 0 \\ -u^2 + \frac{1}{2}\left(u^2+v^2\right)(\gamma-1) & -u(-3+\gamma) & -v(\gamma-1) & \gamma-1 \\ -uv & v & u & 0 \\ \frac{-c^2 u}{(\gamma-1)} + \frac{u\left(u^2+v^2\right)(2-\gamma)}{2} & \frac{c^2}{\gamma-1} - \frac{-v^2+u^2(-3+2\gamma)}{2} & -uv(\gamma-1) & u\gamma \end{bmatrix} \tag{32}$$

$$A_x M = \frac{\partial F_x}{\partial U}\frac{\partial U}{\partial V} = \frac{\partial F_x}{\partial V} = \begin{bmatrix} u & u^2 & uv & \frac{1}{2}uv^2 \\ \rho & 2\rho u & \rho v & \rho(H+u^2) \\ 0 & 0 & \rho u & \rho uv \\ 0 & 1 & 0 & \frac{u\gamma}{(\gamma-1)} \end{bmatrix} \tag{33}$$

Transformation matrix M in two dimensions:

$$\begin{aligned} M &= \frac{\partial U}{\partial V} = \begin{bmatrix} 1 & 0 & 0 & 0 \\ u & \rho & 0 & 0 \\ v & 0 & \rho & 0 \\ \frac{\vec{v}^2}{2} & \rho u & \rho v & \frac{1}{\gamma-1} \end{bmatrix} \\ M^{-1} &= \frac{\partial V}{\partial U} = \begin{bmatrix} 1 & 0 & 0 & 0 \\ -u/\rho & 1/\rho & 0 & 0 \\ -v/\rho & 0 & 1/\rho & 0 \\ \frac{\vec{v}^2}{2}(\gamma-1) & -u(\gamma-1) & -v(\gamma-1) & (\gamma-1) \end{bmatrix} \end{aligned} \tag{34}$$

Diagonalization of the Euler Jacobian:

$$\Delta = L^{-1} M^{-1} \left(\vec{A} \cdot \vec{n} \right) M L$$

$$L = \frac{\partial W}{\partial V} = \begin{bmatrix} 1 & 0 & \frac{\rho}{2c} & \frac{\rho}{2c} \\ 0 & n_y & \frac{n_x}{2} & \frac{-n_x}{2} \\ 0 & -n_x & \frac{n_y}{2} & \frac{-n_y}{2} \\ 0 & 0 & \frac{\rho}{2c} & \frac{\rho}{2c} \end{bmatrix} \tag{35}$$

$$\Delta = \begin{bmatrix} \vec{v} \cdot \vec{n} & 0 & 0 & 0 \\ 0 & \vec{v} \cdot \vec{n} & 0 & 0 \\ 0 & 0 & (\vec{v} \cdot \vec{n} + c) & 0 \\ 0 & 0 & 0 & (\vec{v} \cdot \vec{n} - c) \end{bmatrix}$$